



Gaia GraL: Gaia DR2 Gravitational Lens Systems. VII. XMM-Newton Observations of Lensed Quasars

Thomas Connor^{1,21} , Daniel Stern¹ , Alberto Krone-Martins² , S. G. Djorgovski³ , Matthew J. Graham³ , Dominic J. Walton⁴ , Ludovic Delchambre⁵ , Christine Ducourant⁶ , Ramachrisna Teixeira⁷ , Jean-François Le Campion⁶, Jakob Sebastian den Brok⁸ , Dougal Dobie^{9,10} , Laurent Galluccio¹¹ , Priyanka Jalan¹² , Sergei A. Klioner¹³ , Jonas Klüter¹⁴ , Ashish A. Mahabal^{3,15} , Vibhore Negi¹² , Anna Nierenberg¹⁶ , Quentin Petit⁶, Sergio Scarano Jr^{17,22} , Eric Slezak¹⁸, Dominique Sluse⁵ , Carolina Spindola-Duarte⁷ , Jean Surdej^{5,19} , and Joachim Wambsganss²⁰

¹ Jet Propulsion Laboratory, California Institute of Technology, 4800 Oak Grove Drive, Pasadena, CA 91109, USA; thomas.p.connor@jpl.nasa.gov

² Donald Bren School of Information and Computer Sciences, University of California, Irvine, Irvine CA 92697, USA

³ Division of Physics, Mathematics, and Astronomy, Caltech, Pasadena, CA 91125, USA

⁴ Institute of Astronomy, University of Cambridge, Madingley Road, Cambridge CB3 0HA, UK

⁵ Space sciences, Technologies and Astrophysics Research (STAR) Institute, University of Liège, Belgium

⁶ Laboratoire d'Astrophysique de Bordeaux, Univ. Bordeaux, CNRS, B18N, allée Geoffroy Saint-Hilaire, F-33615 Pessac, France

⁷ Instituto de Astronomia, Geofísica e Ciências Atmosféricas, Universidade de São Paulo, Rua do Matão, 1226, Cidade Universitária, 05508-900 São Paulo, SP, Brazil

⁸ Argelander-Institut für Astronomie, Universität Bonn, Auf dem Hügel 71, D-53121 Bonn, Germany

⁹ Centre for Astrophysics and Supercomputing, Swinburne University of Technology, Hawthorn, Victoria, Australia

¹⁰ ARC Centre of Excellence for Gravitational Wave Discovery (OzGrav), Hawthorn, Victoria, Australia

¹¹ Université Côte d'Azur, Observatoire de la Côte d'Azur, CNRS, Laboratoire Lagrange, Bd de l'Observatoire, CS 34229, F-06304 Nice cedex 4, France

¹² Aryabhata Research Institute of Observational Sciences (ARIES), Manora Peak, Nainital, 263002 India

¹³ Lohrmann-Observatorium, Technische Universität Dresden, D-01062 Dresden, Germany

¹⁴ Department of Physics and Astronomy, Louisiana State University, Baton Rouge, LA 70803 USA

¹⁵ Center for Data Driven Discovery, California Institute of Technology, Pasadena, CA 91125, USA

¹⁶ Department of Physics, University of California Merced, 5200 North Lake Road, Merced, CA 95343, USA

¹⁷ Departamento de Física—CCET, Universidade Federal de Sergipe, Rod. Marechal Rondon s/n, 49.100-000, Jardim Rosa Elze, São Cristóvão, SE, Brazil

¹⁸ Université Côte d'Azur, Observatoire de la Côte d'Azur, CNRS, Laboratoire Lagrange, Boulevard de l'Observatoire, CS 34229, F-06304 Nice, France

¹⁹ Astronomical Observatory Institute, Faculty of Physics, Adam Mickiewicz University, ul. Słoneczna 36, 60-286 Poznań, Poland

²⁰ Zentrum für Astronomie der Universität Heidelberg, Astronomisches Rechen-Institut, Mönchhofstr. 12-14, D-69120 Heidelberg, Germany

Received 2021 September 28; revised 2021 December 14; accepted 2021 December 15; published 2022 March 3

Abstract

We present XMM-Newton X-ray observations of nine confirmed lensed quasars at $1 \lesssim z \lesssim 3$ identified by the Gaia Gravitational Lens program. Eight systems are strongly detected, with 0.3–8.0 keV fluxes $F_{0.3-8.0} \gtrsim 5 \times 10^{-14} \text{ erg cm}^{-2} \text{ s}^{-1}$. Modeling the X-ray spectra with an absorbed power law, we derive power-law photon indices and 2–10 keV luminosities for the eight detected quasars. In addition to presenting sample properties for larger quasar population studies and for use in planning for future caustic-crossing events, we also identify three quasars of interest: a quasar that shows evidence of flux variability from previous ROSAT observations, the most closely separated individual lensed sources resolved by XMM-Newton, and one of the X-ray brightest quasars known at $z > 3$. These sources represent the tip of the discoveries that will be enabled by SRG/eROSITA.

Unified Astronomy Thesaurus concepts: Quasars (1319); Strong gravitational lensing (1643); X-ray astronomy (1810); X-ray quasars (1821); Scaling relations (2031)

Supporting material: figure set

1. Introduction

Strong gravitational lensing, wherein a distant object is magnified and possibly resolved into multiple images by a massive foreground structure, is an extremely valuable tool for studying the universe (see Treu 2010 for a review). Not only do strong lenses enable mass reconstruction from the scales of galaxy clusters (e.g., Paterno-Mahler et al. 2018) to the scales of galaxy subhaloes (e.g., Vegetti et al. 2012), but strong lensing measurements have enabled tests of fundamental physics and cosmology. Using spatially resolved kinematic measurements of

lensed arcs, Collett et al. (2018) tested the predictions of general relativity in the strong-gravity regime. Furthermore, a number of works have exploited time delays between individual images to calculate H_0 (e.g., Suyu et al. 2017; Chen et al. 2018; Vega-Ferrero et al. 2018).

Of particular importance in the strong lensing regime are background quasars lensed by galaxy-scale masses. Quasar microlensing directly constrains the stellar mass fraction at the position of lensed images, enabling kinematics-independent derivations of dark matter fractions in galaxies (Bate et al. 2011; Oguri et al. 2014). Furthermore, using flux measurements of lensed quasars to model the mass distribution of lensing galaxies, works including those of Gilman et al. (2020) and Nierenberg et al. (2020) have constrained the characteristics of dark matter structures. And, building on the work of Kochanek & Dalal (2004), which showed that microlensing time delays can enable a measurement of lensed source sizes, multiple works have exploited lensing to measure the properties of quasars (e.g., Wayth

²¹ NPP Fellow.

²² IAG-USP Fellow.

et al. 2005; Pooley et al. 2007). Due to the vast utility of these sources, lensed quasars have remained compelling targets for discovery.

While the first lensed quasars were discovered by serendipity (Walsh et al. 1979), exploiting the full potential of these systems requires both large samples and systematic searches. To that end, the Gaia Gravitational Lenses working group (GraL) has exploited the exquisite astrometric precision of the Gaia mission (Gaia Collaboration et al. 2016) to identify candidate lensed quasars (Krone-Martins et al. 2018, Paper I). Ducourant et al. (2018, Paper II) expanded on this work by creating an exhaustive list of known quasars and integrating in the submilliarcsecond astrometry of Gaia Data Release 2 (Gaia Collaboration et al. 2018). Following refinement of the candidate selection algorithms (Delchambre et al. 2019, Paper III) and a demonstration of the potential for Gaia observations alone to constrain mass models (Wertz et al. 2019, Paper IV), Krone-Martins et al. (2019, Paper V) and Stern et al. (2021, Paper VI) spectroscopically confirmed a set of doubly and quadruply imaged quasars, respectively. All told, over two dozen lensed quasars have been identified and confirmed by GraL, which is one of several ongoing searches for lensed quasars (Ostrovski et al. 2017, 2018; Agnello et al. 2018; Lemon et al. 2018, 2019, 2020; Treu et al. 2018; Khramtsov et al. 2019; Li et al. 2020).

As new gravitational lens systems are discovered, they become intriguing targets for X-ray studies, enabling discoveries beyond those of optical investigations. In particular, as noted by Pooley et al. (2012), a quiescent lensing galaxy does not contribute a meaningful amount of X-ray flux, allowing for improvements in mass modeling. Utilizing the inherent ability to obtain spectral information from each resolved image, Walton et al. (2015), building on measurements at lower redshifts (Reis et al. 2014; Reynolds et al. 2014), demonstrated the ability of X-ray observations of lensed quasars to measure black hole spins in the $z > 3$ universe. Differences between X-ray and optical light curves have enabled multiple measurements of the size of the X-ray emitting region in lensed quasars (e.g., Morgan et al. 2008; Dai et al. 2010; Mosquera et al. 2013). In addition, while distant quasars can still be well-studied from optical to radio wavelengths (e.g., Bañados et al. 2021), even luminous quasars with deep X-ray observations are so photon-limited as to preclude all but the most basic of spectral analyses (e.g., Connor et al. 2019); as such, the boost in flux caused by lensing that enables more detailed studies of individual objects is critical in the X-ray regime for exploring the $z > 3$ universe.

Of particular interest are microlensing events when lensed objects touch a caustic. These caustic-crossing events have been previously observed to produce magnifications in excess of $\times 2000$ (Kelly et al. 2018). While such extreme magnification events are uncommon and generally associated with the macrocaustics of galaxy clusters (Diego 2019), even smaller-magnification microlensing events could enable studies of distant quasars at a level of detail otherwise only obtainable in the local universe (e.g., Tomozeiu et al. 2018). As the strength of a caustic-crossing event increases with decreasing source size, the relatively small scale of X-ray emitting regions makes this energy band ideal for exploiting these incidents. Mosquera & Kochanek (2011) found that the median Einstein radius crossing time for a sample of 87 lensed quasars, which is equivalent to the rate of caustic-crossing events, was once per 20 yr per lensed image. Due to the rarity of these events, analyses often rely on photometric monitoring of low-magnification events (e.g., Courbin et al. 2018; Fian et al. 2018) or

of statistical analyses of higher-magnification events (e.g., Rodney et al. 2018). However, with time-domain surveys such as the Zwicky Transient Facility (Bellm et al. 2019) providing deep coverage of large fractions of the sky at near-daily cadence, we may soon be able to detect caustic-crossing events early and often enough to enable target of opportunity observations. Preliminary X-ray observations are necessary to prioritize these optically selected events for X-ray follow-up.

In this article, we present the X-ray observations and analysis of a subset of the Gaia GraL sample. The paper is structured as follows: we present our observations and their reduction in Section 2, provide the results in Section 3, discuss these results in the broader context of ongoing studies in Section 4, and summarize this effort in Section 5. Throughout this work, we adopt a flat cosmology with $H_0 = 70 \text{ kms}^{-1} \text{ Mpc}^{-1}$, $\Omega_M = 0.3$, and $\Omega_\Lambda = 0.7$. All uncertainties are given at the 1σ level and all upper limits correspond to 3σ values. Except where otherwise stated, all luminosities presented in this work are not corrected for the lensing magnification.

2. X-Ray Observations and Analysis

We proposed a snapshot survey using XMM-Newton to observe a sample of 19 lensed quasars from GraL (PropID: 086462, PI: Stern), though this survey was accepted as C Priority, and so only a random subsample was observed. In total, 10 new quasars were observed in this program, the details of which are given in Table 1. One unlensed quasar—SDSS J1141–0436—was included in this sample. Though initial reductions of follow-up spectroscopy suggested a lensed quasar, subsequent analysis revealed this source to be an asterism composed of a Galactic star and a quasar (Paper VI).

Each target was observed for around 10 ks with the European Photon Imaging Camera (EPIC) on XMM-Newton (Jansen et al. 2001), consisting of two MOS cameras (Turner et al. 2001) and a pn CCD camera (Strüder et al. 2001). Sources were positioned at the standard EPIC-pn prime position, ensuring they were away from pn chip edges. Camera readout was conducted in full frame mode, and we used the thin optical blocking filter.

Observations were conducted from 2020 July to 2021 April; details of these observations are given in Table 2. We note that there are three additional OBSIDs associated with our program that are not included in this analysis. Two of these observations (0864622301 and 0864622401) were conducted with the EPIC filter wheel in the closed position, due to enhanced radiation at the start of a revolution, while the third (0864621401) was affected by radiation at such a significant amount as to be unusable. Several other observations were also affected by radiation, as indicated in Table 2, but at a level that still allowed the data to be usable. We also note those sources for which the pn camera experienced a full scientific buffer. Normally caused by a high-radiation background, the full scientific buffer causes the pn camera to switch to counting mode, thereby no longer recording scientific data.

We reduced and processed these observations using the Scientific Analysis System (SAS; Gabriel et al. 2004) v19.0.0. To standardize our analysis, we used the `xmextractor` script to produce event files and extract spectra. As part of this analysis, we adopted standard analysis flags (`PATTERN` ≤ 12 for MOS and `PATTERN` ≤ 4 for pn) and good time intervals (`RATE` ≤ 0.35 for MOS and `RATE` ≤ 0.4 for pn). Source spectra were extracted in `xmextractor`-selected apertures,

Table 1
Target Properties and XMM-Newton Observations

Target	R.A.	Decl.	z	μ^a	Separation ^b	Notes
GraL J0659+1629	06:59:04.1	+16:29:09	3.083	37.6	6''8	quad - Paper VI
GraL J0818–2613	08:18:28.3	–26:13:25	2.164	100.1	6''2	quad - Paper VI
GraL J1131–4419	11:31:00.0	–44:20:00	1.090	70.4	1''6	quad - Paper VI
GraL J1651–0417	16:51:05.3	–04:17:25	1.451	7.3	10''1	quad - Paper VI
GraL J1719+1515	17:19:22.6	+15:15:46	1.716	...	1''1	double - Paper V
GraL J1817+2729	18:17:30.8	+27:29:40	3.074	19.0	1''8	quad - Paper VI
GraL J2017+6204	20:17:49.1	+62:04:43	1.724	14.7	0''7	quad - Paper VI
GraL J2103–0850	21:03:29.0	–08:50:49	2.455	13.3	1''0	quad - Paper VI
GraL J2200+1448	22:00:15.6	+14:49:00	1.115	...	2''5	double - Paper V
SDSS J1141–0436	11:41:03.9	–04:36:51	1.647	unlensed - Paper VI

Notes.

^a Adopted magnification based on SIS + γ models presented in Paper VI (Quads).

^b For the quads, separation corresponds to the maximum separation.

Table 2
Observations and Fluxes

Target	OBSID	Start Date (YYYY-mm-dd)	Exp. (ks)	Count Rate ^a			$F_{0.3-8.0}$ (10^{-14} erg cm ⁻² s ⁻¹)
				MOS1	MOS2 (ct ks ⁻¹)	pn	
GraL J0659+1629	0864620401	2021-Apr-07	16.7	55.5 ± 2.7	44.8 ± 2.4	173 ± 11	56.3 ^{+3.2} _{-3.0}
GraL J0818–2613	0864620501	2020-Oct-23	8.5	26.5 ± 2.0	21.7 ± 1.9	60.8 ± 4.5	38.0 ^{+4.3} _{-4.0}
GraL J1131–4419	0864620701 ^{b,c}	2020-Dec-11	16.1	33.1 ± 3.7	32.1 ± 3.3	...	33.2 ^{+4.7} _{-3.5}
GraL J1651–0417	0864621301 ^{b,c}	2021-Mar-17	17.4	36.0 ± 2.1	39.4 ± 2.1	...	42.1 ^{+2.9} _{-2.7}
GraL J1719+1515	0864622501 ^c	2021-Mar-02	11.0	8.9 ± 1.5	13.4 ± 1.7	39.4 ± 4.5	11.8 ^{+1.8} _{-1.4}
GraL J1817+2729	0864621501 ^{b,c}	2020-Oct-24	19.5	<6.1	<4.4	...	<17.30
GraL J2017+6204	0864621701	2020-Jul-09	15.3	6.9 ± 0.9	5.7 ± 0.8	17.6 ± 2.3	11.8 ^{+2.1} _{-1.8}
GraL J2103–0850	0864621901 ^c	2020-Nov-05	14.2	11.5 ± 1.4	12.6 ± 1.3	...	15.5 ^{+2.0} _{-2.1}
GraL J2200+1448	0864622001 ^c	2020-Nov-17	12.3	6.7 ± 1.5	8.4 ± 1.4	...	8.59 ^{+1.74} _{-1.45}
SDSS J1141–0436	0864620801 ^{b,c}	2020-Dec-25	15.7	<10.9	<8.2	...	<16.52

Notes.

^a Background-subtracted count rate from 0.3–8.0 keV.

^b Affected by radiation.

^c pn experienced full scientific buffer during observation.

while background spectra were extracted from off-source circular apertures of varying size.

Spectral fitting was performed using the Python implementation of XSPEC v12.11.1 (Arnaud 1996). We used a simple absorbed power-law model to fit our sources (phabs×powerlaw). For all targets, we adopt a Galactic neutral hydrogen column density, N_{H} , based on the HI HI4PI Survey (HI4PI Collaboration et al. 2016). Both the normalization of the power law and the photon index, Γ , were free to vary. We fixed the spectra of all three EPIC cameras to the same normalization, as studies with significantly deeper spectra have found that cross-normalization terms are effectively unity (e.g., Read et al. 2014; Li et al. 2015). We binned our spectra to a minimum of only one count per bin, and we therefore used the modified C -statistic to evaluate best fits and errors (Cash 1979; Wachter et al. 1979).

Additionally, we fit each source including an absorption component at the quasar redshift (phabs×powerlaw×z-phabs). Two sources have a redshifted column density, $N_{\text{H},z}$, that is not consistent with 0; for the other objects, we only report the results of the simpler fits. These two sources—GraL J0818

–2613 and GraL J2017+6204—were previously identified in Paper VI as having optical spectral signatures of absorption. GraL J0818–2613 has a red continuum and weak Ly α emission, while GraL J2017+6204’s spectrum is reddened with broad absorption line (BAL) features. The only other quasar in our sample with optical features of absorption is GraL J1817+2729, which is not strongly detected in our observations.

We computed the uncertainties on fit parameters by measuring contours in the C statistic. As noted by Cash (1979), ΔC behaves as $\Delta\chi^2$ when evaluating confidence intervals, such that the 1σ uncertainties include those fits where $\Delta C \leq 2.30$ (or $\Delta C \leq 3.53$ for the three-component model; see, e.g., Lampton et al. 1976). Figure 1, presenting GraL J0659+1629, shows an example of our reduced data. The combined images from the three EPIC cameras are shown in the left, smoothed with a Gaussian kernel of width $\sigma = 4''0$ and with individual normalizations adjusted for presentation purposes. On the right, we show the background-subtracted combined count rate spectra from all three cameras, binned for plotting purposes. Horizontal bars show the source count rate, with thinner bars above and below corresponding to the 1σ uncertainties, using the methods of Gehrels (1986). The

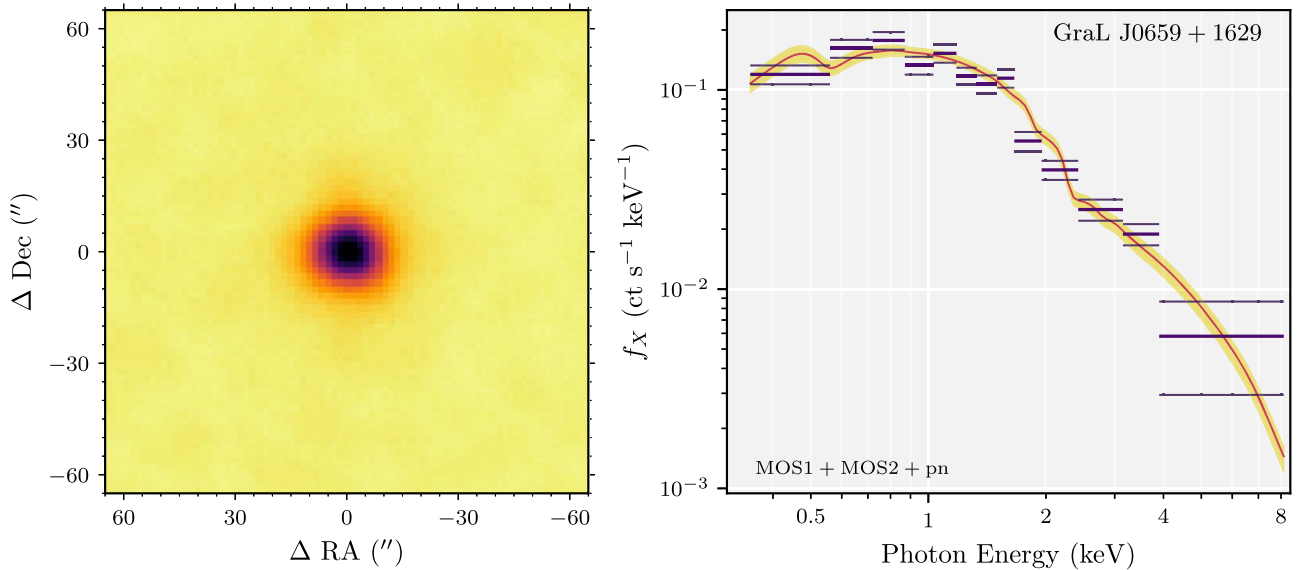


Figure 1. EPIC observations of GraL J0659+1629. Left: imaging observations in the combined three EPIC cameras, covering 0.3–8.0 keV. This image is centered on GraL J0659+1629 and has been smoothed with a Gaussian kernel of width $\sigma = 4''$ and binned to pixels of width $1''75$. Right: combined background-subtracted spectra from the three EPIC instruments, binned for plotting purposes, overlaid on the best-fit model and its 1σ uncertainties (yellow). More detailed versions of this figure for the entire sample are presented in the Appendix in Figures 5 and 6.

best-fit model and its 1σ uncertainties were folded through the spectral responses with XSPEC and are plotted with the red line and yellow region, respectively. More detailed versions of this figure are presented for each quasar in our sample in the Appendix as Figures 5 and 6.

3. Results

In this section, we present the results of our analysis of the 10 observed quasars. We first present the observed properties for the entire sample in Section 3.1, including notes on specific parameters. Then, in Section 3.2, we discuss individual quasars, including how results may be influenced by the observing conditions.

3.1. Full Sample

We begin our analysis of these quasars with measurements of their flux. As with all results reported here, we do not attempt to differentiate the properties of individual quasar images, as the XMM-Newton EPIC half energy width is $\sim 15''$. One motivation for reporting flux values is to facilitate the planning of future observations of these sources in the event of a caustic-crossing event. As these observations may be conducted with either Chandra or XMM-Newton, we present flux values in the range of 0.3–8.0 keV, which is a suitable broad baseline for both observatories. Total energy fluxes, in units of $\text{erg cm}^{-2} \text{s}^{-1}$, are given in Table 2 for all sources. These flux values are derived in XSPEC from the best-fitting model fits. For those quasars that were not well-fit, 3σ upper limits are given instead. We also report the background-subtracted source count rates in Table 2. Upper limits are again given for rates not detected at a 3σ level, and we do not report values for sources observed for less than 1.5 ks in a camera.

Next, we present the fitted X-ray properties of these quasars. The normalization and photon index of each object’s power-law component is listed in Table 3. As with flux measurements, we present the upper limits on the normalization for the two quasars that were not detected. We also present the unobscured,

rest-frame 2–10 keV luminosities. These model-derived luminosities assume the source is entirely composed of power-law emission in this energy band. For the two quasars that were well-fit by this model, we also include the constraints on the redshifted column density.

Finally, we include the rest-frame $6\mu\text{m}$ luminosity for each of these objects. Following, e.g., Stern (2015), we use photometry from the Wide-field Infrared Survey Explorer (WISE; Wright et al. 2010) and known redshifts from Paper IV, Paper V, and Paper VI to calculate $\nu L_{6\mu\text{m}}$. For our entire sample, rest-frame $6\mu\text{m}$ lies between the WISE W3 ($12\mu\text{m}$) and W4 ($24\mu\text{m}$) channels, and we compute luminosities through linear interpolation of these values. IR luminosities are listed in Table 3. Unlike the X-ray measurements, which are expected to only have minimal contamination from the lensing galaxy, these values could potentially be slightly boosted in flux due to the contribution of the intervening galaxy. On the other hand, lensing preferentially occurs from more massive (i.e., early-type) galaxies, which have falling spectral energy distributions beyond rest-frame H -band, so the expectation is that the W3 and W4 flux from these systems is dominated by the lensed quasar emission.

We show the distribution of X-ray to IR luminosities for this sample in Figure 2. For all lensed quasars, we also plot a magnification track, showing what these values would be were the quasar unlensed. For the quad lenses, we use the modeled magnification values from Paper VI (listed in Table 1), while we adopt a value of $\mu = 5$ for the doubly imaged lenses (a typical value for these systems; see, e.g., Kochanek et al. 2000; Rusu et al. 2016). Also shown is the relation between X-ray and IR luminosities presented by Stern (2015). While linear at lower luminosities, this relation has a characteristic flattening above $\nu L_{6\mu\text{m}} \sim 10^{44} \text{ erg s}^{-1}$, believed to be caused by the X-ray emission saturating as the corona cools and softens with increasing thermal emission from the disk (e.g., Brightman et al. 2013). We also include a sample of archival lensed quasars (Just et al. 2007; Stern & Walton 2020; Walton et al., submitted), local Seyferts (Horst et al. 2008; Gandhi et al. 2009), and luminous quasars (Just et al. 2007). For the lensed

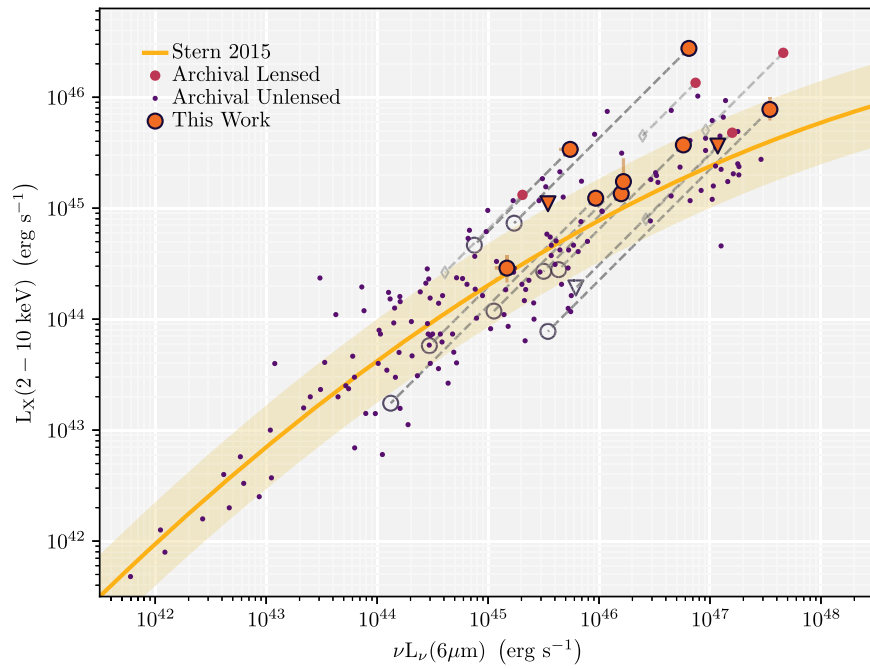


Figure 2. Rest-frame, absorption-corrected 2–10 keV X-ray luminosity against rest-frame 6 μm luminosity for the quasars analyzed in this work (orange), as well as a sample of archival lensed and unlensed AGN. Upper limits are indicated by downward-pointing triangles. The X-ray to mid-infrared luminosity relation of Stern (2015) is shown by the yellow line. For all lensed quasars, the dashed gray lines indicate their unmagnified luminosities; we assume a magnification of $\mu = 5$ for all quasars without reported magnifications. The sources of archival values are described in the text.

Table 3
Mid-IR Luminosities and X-Ray Properties of the Sample

Target	$\log \nu L_{6\mu\text{m}}$ (erg s^{-1})	N_{H} (10^{20} cm^{-2})	Norm ^a (10^{-5})	Γ	$N_{\text{H},z}$ (10^{22} cm^{-2})	$\log L_{2-10}$ (erg s^{-1})	C/DOF
GraL J0659+1629	$46.81^{+0.03}_{-0.04}$	11.60	$12.83^{+0.63}_{-0.65}$	$1.87^{+0.07}_{-0.07}$...	$46.44^{+0.02}_{-0.02}$	831.18/937
GraL J0818–2613	47.54 ± 0.01	13.40	$6.76^{+2.92}_{-1.92}$	$1.42^{+0.26}_{-0.25}$	$8.07^{+4.21}_{-3.64}$	$45.89^{+0.11}_{-0.10}$	520.04/623
GraL J1131–4419	45.97 ± 0.02	4.86	$7.14^{+0.79}_{-0.83}$	$1.96^{+0.20}_{-0.19}$...	$45.09^{+0.06}_{-0.06}$	282.68/322
GraL J1651–0417	$45.74^{+0.08}_{-0.10}$	9.52	$9.31^{+0.53}_{-0.63}$	$1.88^{+0.09}_{-0.09}$...	$45.53^{+0.02}_{-0.03}$	568.31/682
GraL J1719+1515	46.20 ± 0.02	5.44	$2.63^{+0.28}_{-0.30}$	$1.99^{+0.17}_{-0.17}$...	$45.13^{+0.05}_{-0.05}$	290.77/278
GraL J1817+2729	47.07 ± 0.02	8.43	< 1.59	< 45.56	...
GraL J2017+6204	46.22 ± 0.02	13.40	$2.53^{+2.81}_{-1.19}$	$1.49^{+0.52}_{-0.44}$	$10.96^{+9.00}_{-6.50}$	$45.24^{+0.21}_{-0.17}$	371.22/392
GraL J2103–0850	$46.76^{+0.03}_{-0.04}$	6.02	$2.75^{+0.42}_{-0.31}$	$1.68^{+0.17}_{-0.19}$...	$45.57^{+0.05}_{-0.05}$	292.51/317
GraL J2200+1448	$45.17^{+0.09}_{-0.11}$	4.31	$2.25^{+0.33}_{-0.39}$	$2.43^{+0.36}_{-0.35}$...	$44.46^{+0.12}_{-0.13}$	267.07/279
SDSS J1141–0436	$45.54^{+0.12}_{-0.16}$	3.05	< 2.38	< 45.04	...

Notes.

^a Normalization of the `powerlaw` component, with units $\text{photons s}^{-1} \text{ cm}^{-2} \text{ keV}^{-1}$ at 1 keV.

quasar sample, magnification tracks are for reported values if known, and are otherwise also assumed to be $\mu = 5$.

3.2. Notes on Individual Quasars

3.2.1. GraL J0659+1629

The highest-redshift quasar in our sample, GraL J0659+1629, is also the X-ray brightest. Consequently, this quasar is the most X-ray luminous object in our sample by almost an order of magnitude. Paper VI reported that there are no archival radio sources associated with this source, and the closest object in the 3 GHz Very Large Array Sky Survey Epoch 1 Quick Look catalog is almost two arcminutes away (Gordon et al. 2020). We have also carried out deeper VLA observations (D. Dobie et al., 2021, in preparation) and detected radio sources at

the location of all four optical images with a typical flux density of $\sim 90 \mu\text{Jy}$, comparable to the optical flux density reported by Paper VI. This quasar therefore does not fit the standard definition of radio-loud, i.e., having a radio flux density greater than 10 times its optical flux density (e.g., Kellermann et al. 1989). Conversely, the most X-ray luminous quasars in the $z > 3$ universe tend to be radio-loud quasars or blazars (e.g., Khorunzhev et al. 2021). As such, this source presents a unique opportunity to study the radio-quiet $z > 3$ quasar population in detail. We also note that the high observed X-ray luminosity is potentially indicative of a large magnification; as discussed by Stern (2015), X-ray luminosities tend to saturate above $\sim 10^{44} \text{ erg s}^{-1}$, so the observed value of $10^{46.4} \text{ erg s}^{-1}$ is the result of either a very intrinsically luminous quasar or a large luminosity boost from lensing. From the

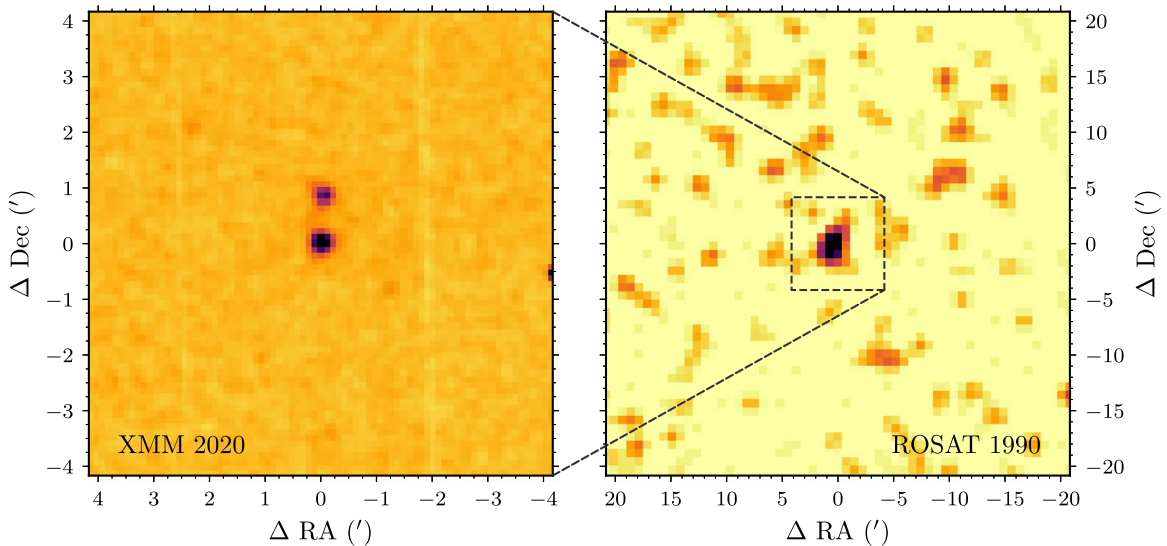


Figure 3. Left: new XMM-Newton image of GraL J1131–4419, taken 2020 December 11. Right: archival ROSAT image of the same quasar, taken 1990 July 7 as part of the ROSAT All Sky Survey. The narrower field of view in the XMM image is indicated by the dashed lines. In the region that produced the large flux in 1990, the only sources in the current observations are GraL J1131–4419 and the nearby star, as discussed in the text.

modeling presented in Paper VI, $\mu = 37.6$, demonstrating the validity of this technique for identifying significantly lensed quasars.

We note that GraL J0659+1629 has also been observed by Chandra, both through Director’s discretionary time (1.67 ks, OBSID: 22018, PI: Pooley) and guest observer time (14.87 ks, OBSID: 23825, PI: Pooley). While the latter was taken only three months prior to our XMM observations (2021 April 07), the former observations were conducted 2019 January 15 and thus enable a check on possible variability. Using CIAO v4.13 (Fruscione et al. 2006) and following standard procedures (Connor et al. 2021), we reduced the earlier Chandra observations and extracted a spectrum of the lensed images in an $8''$ radius aperture. With 83_{-9}^{+11} net counts (Gehrels 1986), the quasar is strongly detected, and a power-law fit finds results similar to those of our XMM spectrum: $\Gamma = 1.7_{-0.2}^{+0.1}$, $\log(L_{2-10}/(\text{erg s}^{-1})) = 46.46_{-0.02}^{+0.01}$, and $F_{0.3-8.0} = 68.6_{-9.0}^{+13.0} \times 10^{-14} \text{ erg s}^{-1} \text{ cm}^{-2}$. These values agree with the XMM results to within mutual uncertainties.

3.2.2. GraL J1131–4419

Voges et al. (2000) report an X-ray source at this position in ROSAT All-Sky Survey observations, 1RXS J113058.9–441949, shown in Figure 3. While that catalog only reports a source count rate, the second ROSAT all-sky source catalog (Boller et al. 2016) includes properties from a power-law spectral fit. The reported absorption-corrected flux in the 0.1–2.4 keV band is $1.6 \times 10^{-11} \text{ erg s}^{-1} \text{ cm}^{-2}$, which is almost two orders of magnitude brighter than what we report here. We note this flux has no reported errors and that it is based only on 18_{-4}^{+5} net counts (Gehrels 1986). Although a source is clearly seen at the position of the lensed quasar in the early image, the flux is derived from spectral fitting of few photons and should therefore have large uncertainties.

Adopting the nominal ROSAT flux, some of the discrepancy with the XMM results can be explained by Boller et al. (2016) effectively adding in flux by correcting for absorption and the differences in energy bands. Further differences may be driven by the fitted power law, which has a best-fit photon index of $\Gamma = 3.07$ for the ROSAT data. As discussed by Connor et al.

(2020), an excessively steep fit to the photon index caused by limited source counts can effect a larger calculated flux at soft energies. Yet Γ cannot be entirely to blame, as the normalization, $n_{2\text{RXS}} = (9.4 \pm 5.4) \times 10^{-4}$, is still an order of magnitude larger than what we find in the more recent XMM-Newton observations.

We also note that another X-ray source is seen in the new X-ray imaging, roughly $50''$ to the north at the location of the high proper motion star 2MASS J11310001–4419088. However, it is unlikely that this is the source of the large ROSAT flux, for two reasons. First, although the separation of the two objects may lead to some flux contamination in the ROSAT imaging (see Boese 2000), the star is fainter than GraL J1131–4419 in the new observations, by around a factor of two, and much fainter than the earlier flux value. Second, 1RXS J113058.9–441949 is only $16''$ from GraL J1131–4419, consistent with the expected positional uncertainty Boller et al. (2016) report for ROSAT coordinates. In contrast, the ROSAT detection is $42''$ from 2MASS J11310001–4419088, implying that the star was not the source of the X-ray flux. There are no further bright X-ray objects within $5'$ of the lensing system.

It is not clear what is responsible for such a change in the observed flux. While AGN are known to have intrinsic flux variations in X-rays (e.g., Paolillo et al. 2004), the observed dimming is too large to be explained by stochastic variability from changes in black hole fueling alone (Sartori et al. 2018). Such a large dimming over 30 yr (15 yr in the source frame) could be attributed to the quasar being a changing-look AGN (Ricci et al. 2020), although this is difficult to assess without a spectrum from the earlier epoch. Serendipitous *Swift* observations from 2009–2012 show no significant difference in the X-ray flux versus what is found here ($f_{0.3-10.0 \text{ keV}} = 6_{-2}^{+1} \times 10^{-13} \text{ erg s}^{-1} \text{ cm}^{-2}$; Evans et al. 2020). Alternatively, the ROSAT observations could have coincided with a microlensing event, although this, too, would be an extreme value for such an effect (Chen et al. 2012).

3.2.3. GraL J1651–0417

This quasar has the largest maximum separation of our sample, at $10''1$ (Paper VI). The most separated lensed image is

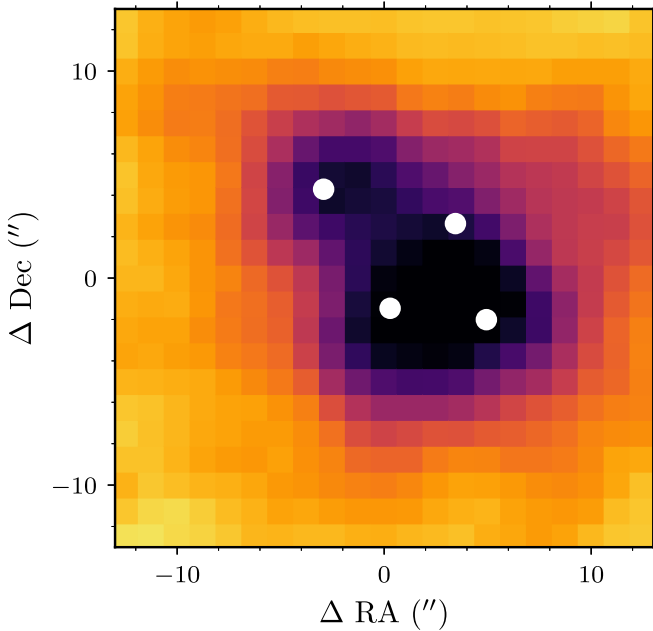


Figure 4. MOS1+MOS2 0.3–8.0 keV image of GraL J1651–0417, smoothed with a Gaussian kernel of width $1''/5$. The positions of the lensed sources, as identified by Paper VI, are indicated by white dots. A small relative offset has been applied to the lensed image positions in this figure, in keeping with the expected pointing accuracy of XMM-Newton. Although the extended wings of these sources overlap, the most distant lensed source can nevertheless be resolved.

located to the NE, while the three other images in this quad are located in close proximity to each other. In the X-ray observations of this system, presented in Figure 4, we find that the quasar is composed of two separate sources, with the second source appearing in the direction and at the separation expected of the NE image. Individual lens images have been resolved by XMM-Newton when the lensing object is a galaxy cluster (e.g., Lamer et al. 2006), but previous observations of sources with galaxy-scale lenses have heretofore been unresolved with this observatory (e.g., Fedorova et al. 2008; Chartas et al. 2016). GraL J1651–0417 is thus a potentially interesting source for future X-ray studies with large effective area but worse-than-arcsecond resolution, such as X-IFU on Athena (Barret et al. 2018).

3.2.4. GraL J1817+2729

Despite having one of the highest inferred $6\ \mu\text{m}$ luminosities of our sample, this gravitational lens system, known as Hercules’ Sword (Paper VI), is undetected in a nominal exposure of 19.5 ks. However, this observation was heavily affected by radiation; the pn camera experienced a full scientific buffer and was rendered unusable for our analysis, while the good time intervals for the MOS cameras only summed to 3.1 and 3.0 ks for MOS1 and MOS2, respectively. Nevertheless, the strict upper limits on measured count rates place this $z = 3.07$ lensed quasar as the faintest target in our sample. From a mass model of the system, Lemon et al. (2019) report a magnification for Hercules’ Sword of $\mu = 14.2^{+1.9}_{-0.9}$, similar to the value of $\mu = 19.0$ derived from Paper VI. Based on that, the unmagnified X-ray luminosity is, at most, of order $10^{44}\ \text{erg s}^{-1}$, while the IR luminosity is still approximately $10^{46}\ \text{erg s}^{-1}$. This value, even at the X-ray limit, is still a large offset from the Stern (2015) relation.

One potential explanation is that the IR luminosity is contaminated in a way the X-ray measurement is not. Paper VI spectroscopically identified a Galactic mid-type star $\sim 2''$ NW of the lens, which is the brightest *I*-band object in the system (Rusu & Lemon 2018). Subaru imaging and associated mass modeling presented by Rusu & Lemon (2018) show that the lensing galaxy is brighter (*I*-band) than two of the lensed images and is suggestive of an edge-on, dusty disk. Neither a typical Galactic star nor an inactive galaxy should be able to mimic such a large IR luminosity, however.

Conversely, the spectrum of this lensed quasar shows strong CIV $\lambda 1549$ BAL features. Previous studies have found that the strength of BAL features correlates with a reduced X-ray luminosity (Gibson et al. 2009). The presence of this correlation in observed hard-energy NuSTAR observations suggests that this faintness is intrinsic, not caused by absorption, and so would still be present even at $z = 3$ (Luo et al. 2014). BAL quasars can be more luminous than the limit set for Hercules’ Sword—Vito et al. (2018) reported on XMM-Newton observations of five $z \sim 2$, $M_{\text{BH}} \sim 10^{10} M_{\odot}$ quasars with BAL features, finding luminosities of $L_{2-10} \gtrsim 10^{45}\ \text{erg s}^{-1}$, while Connor et al. (2020) reported on an unlensed $M_{\text{BH}} = 3 \times 10^9 M_{\odot}$, $z = 6.59$ BAL quasar with $L_{2-10} \sim 6 \times 10^{44}\ \text{erg s}^{-1}$. However, the faintness of GraL J1817+2729 is still in keeping with the expectation of an X-ray weak quasar.

3.2.5. GraL J2103-0850

This gravitational lens system is associated with a source detected in the ROSAT All-Sky Faint Source Catalog (Voges et al. 2000), 1RXS J210328.9–085039. In the second ROSAT all-sky source catalog, Boller et al. (2016) report an absorption-corrected 0.1–2.4 keV flux from an assumed power-law model of $F_{2\text{RXS}} = 33 \times 10^{-14}\ \text{erg s}^{-1}\ \text{cm}^{-2}$. Considering the slightly softer energy range of this observation and the correction for absorption, this value is consistent with what we report here, suggesting only a minimal amount of variation since the ROSAT observations of 1990/1991.

4. Discussion

In their analysis of MG 1131+0456, Stern & Walton (2020) proposed that the $L_X - \nu L_{\nu}(6\ \mu\text{m})$ relation could act as a means to identify lensed quasars. As shown in Figure 2, magnification pushes sources on the Stern (2015) relation up and off; thus, any sources with anomalously high X-ray luminosities for their mid-infrared luminosity could indicate lensing. However, most of the sources analyzed here are consistent with the Stern (2015) relation, within the expected scatter. The lack of excess X-ray luminosity is most likely a result of some combination of small magnification factors, intrinsic X-ray luminosities lying below the relation, and the roughly linear correlation at lower luminosities minimizing the impact of magnification on producing deviations. While X-ray luminosity offsets should nevertheless serve as a means of identifying lensing among the most luminous quasars and the strongest magnification lenses, as is demonstrated here by GraL J0659+1629, we should not expect the overall population of lensed sources to only be outliers.

One of the motivations for this work was to establish a baseline set of flux measurements of lensed quasars to facilitate future observations of caustic-crossing events. The full all-sky survey of SRG/eROSITA (eRASS) is expected to reach a

point-source sensitivity of $f_{\text{eRASS}} \lesssim 10^{-14} \text{ erg s}^{-1} \text{ cm}^{-2}$ (Predehl et al. 2021). As such, we expect all of the lens systems presented here to be detected by the full survey and the brightest of these to potentially have multiple observations to constrain their variability. However, that is the limiting sensitivity for detection; even the simple spectral analyses reported here will be beyond the capabilities of the eRASS. As such, future observations of lensed quasars with XMM-Newton and Chandra are still warranted.

Another potential advantage of the SRG-based observatories comes in their potential to detect X-ray variability. The medium-energy ART-XC telescope on SRG is performing daily scans of the sky at 4–12 keV. These scans have sensitivities of $\sim 2 \times 10^{-11} \text{ erg s}^{-1} \text{ cm}^{-2}$ and survey roughly 1% of the sky every day (Sunyaev et al. 2021). It is possible—albeit unlikely—that a caustic-crossing event could produce the magnifications necessary to boost one of the lensed quasars in this sample into that flux threshold. As previous transient sources detected by ART-XC have also been seen by eROSITA (e.g., Mereminskiy et al. 2020; Schwöpe et al. 2020), we would expect similar results from the softer survey. As further gravitational lenses are spectroscopically confirmed, archival observations may reveal past extreme magnification events.

Finally, we note the potential for XMM-Newton in the study of distant lensed quasars. Chandra, with its exquisite angular resolution enabling the separation of individual sources, is often used for studies of lensed quasars (e.g., Chen et al. 2012; Guerras et al. 2017; Dogruel et al. 2020). However, for faint sources, Chandra will be unable to detect the necessary amount of photons for a temporal analysis without deep observations; meanwhile, as demonstrated by Paper II, Gaia observations can provide precise astrometry, obviating that requirement from X-ray observations. In cases such as these, when only spectral information is desired at X-ray energies, XMM-Newton is more than suited for the task.

5. Summary

We have presented XMM-Newton X-ray observations of nine lensed quasars and one unlensed source selected by Gaia GraL. Observations were relatively short (<20 ks), and represent an exploratory program into the nature of the GraL sample. The primary results of this work are as follows.

1. We report X-ray fluxes and XMM-Newton EPIC count rates for eight of the lensed quasars, as well as upper limits for the ninth. Most sources have fluxes of $F_{0.3-8.0} \approx 10^{-13} \text{ erg s}^{-1} \text{ cm}^{-2}$ and count rates of at least 10 ct ks⁻¹ in each MOS camera. These measurements will be invaluable in planning future targeted observations of caustic-crossing events.
2. Using XSPEC, we fit the observed quasars with an absorbed power-law, and we report the best-fit values of this in Table 3. From these fits, we also derive rest-frame 2–10 keV unabsorbed luminosities. Here, we find that the observed sample covers over two orders of magnitude in X-ray luminosity.
3. Despite observing it for almost 20 ks, we do not detect GraL J1817+2729, one of the two most IR luminous quasars in our sample. This is partially due to severe radiation effects during the observation, which cut the effective exposure time to 3 ks in the MOS cameras and which overwhelmed the pn camera entirely. However, the

upper limit we infer from these limited observations nevertheless reveals that this quasar is X-ray faint, perhaps related to its observed BAL features. Due to the lensing magnification, deeper observations may enable the first detailed look at an X-ray faint quasar in the early universe ($z > 3$).

4. We observe GraL J1131–4419, which was previously detected in the ROSAT All-Sky Survey. The X-ray flux reported from that survey is almost two orders of magnitude brighter than what we find here. As the ROSAT observations were taken 30 yr prior to the XMM-Newton observations, it is not entirely clear what the cause of the variability is, but this could potentially be indicative of a major microlensing event in the older observations.
5. MOS observations of GraL J1651–0417 reveal an extended structure to the NE of the main component of the quasar emission. Using a small smoothing scale, we are able to observe two distinct structures in this lens system, in the orientation expected from the Gaia-observed positions of the lensed images. With a maximum separation of 10''/1, this is the most closely separated gravitational lens system resolved into multiple components by XMM-Newton.

The work of T.C. and D.S. was carried out at the Jet Propulsion Laboratory, California Institute of Technology, under a contract with NASA. T.C.'s research was supported by an appointment to the NASA Postdoctoral Program at the Jet Propulsion Laboratory, California Institute of Technology, administered by Universities Space Research Association under contract with NASA. S.G.D. and M.J.G. acknowledge a partial support from the NASA ADAP grant 16-ADAP16-0232, and the NSF grant AST-1815034. D.J.W. acknowledges support from the Science and Technology Facilities Council (STFC) in the form of an Ernest Rutherford Fellowship (grant ST/N004027/1). L.D. acknowledges support from the ESA PRODEX Programme ‘‘Gaia-DPAC QSOs’’ and from the Belgian Federal Science Policy Office. S.A.K. was partially supported by the German Aerospace Agency (grant 50QG1402). D.S. acknowledges support from the European Research Council (ERC) under the European Union’s Horizon 2020 research and innovation programme (grant agreement No. 787886).

Based on observations obtained with XMM-Newton, an ESA science mission with instruments and contributions directly funded by ESA Member States and NASA.

Facility: XMM.

Software: CIAO (Fruscione et al. 2006), PyFITS (Barrett & Bridgman 1999), SAS (Gabriel et al. 2004), XSPEC (Arnaud 1996).

Appendix A

EPIC Observations and Spectral Fits of the Sample

To assist in the planning of future observations of these quasars should they be the site of a future microlensing event, we present full details of our fits and analysis in Figures 5 and 6. In the upper left panels, we show the individual images from the three EPIC cameras, as well as a combined view of all three. These images are 130'' on a side, are centered on the position of the quasar, and are smoothed with Gaussian kernels of width 4''/0. In the upper right, we show contours of the best-

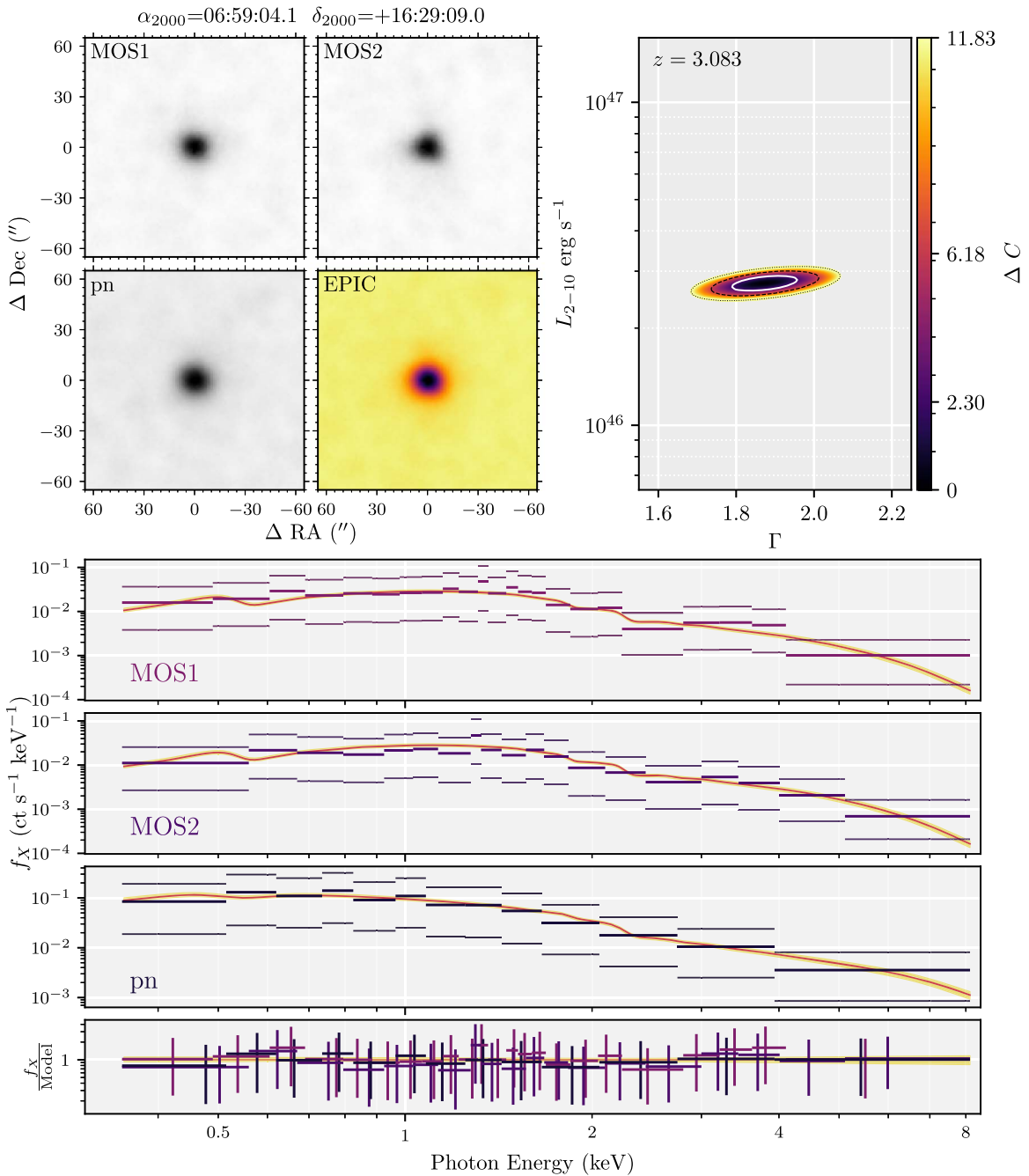


Figure 5. EPIC observations of GrL J0659+1629. The description of the panels is given in the text. The complete figure set (eight images) is available in the online Journal.

(The complete figure set (eight images) is available.)

fitting values of Γ and L_X . Contours corresponding to 1σ , 2σ , and 3σ are indicated by the white, black dashed, and black dotted lines, respectively. For the two quasars well-fit by including a redshifted absorption component, these contours trace the lowest value of ΔC for a given pair of Γ and luminosity across the entire range of modeled column densities.

In the bottom panels of Figure 5, we show the individual observed and best-fitting spectra in the three EPIC cameras, as

well as the residuals. Observed spectra are background-subtracted and have been binned for presentation purposes. Thin horizontal lines above and below the observed values correspond to 1σ uncertainties. Best-fit models, propagated through `fakeit` in XSPEC, are shown by the red lines, while yellow regions trace the bounds of 1σ uncertainties on the fit. For the pn observations that were unusable, the subfigure is rendered in gray.

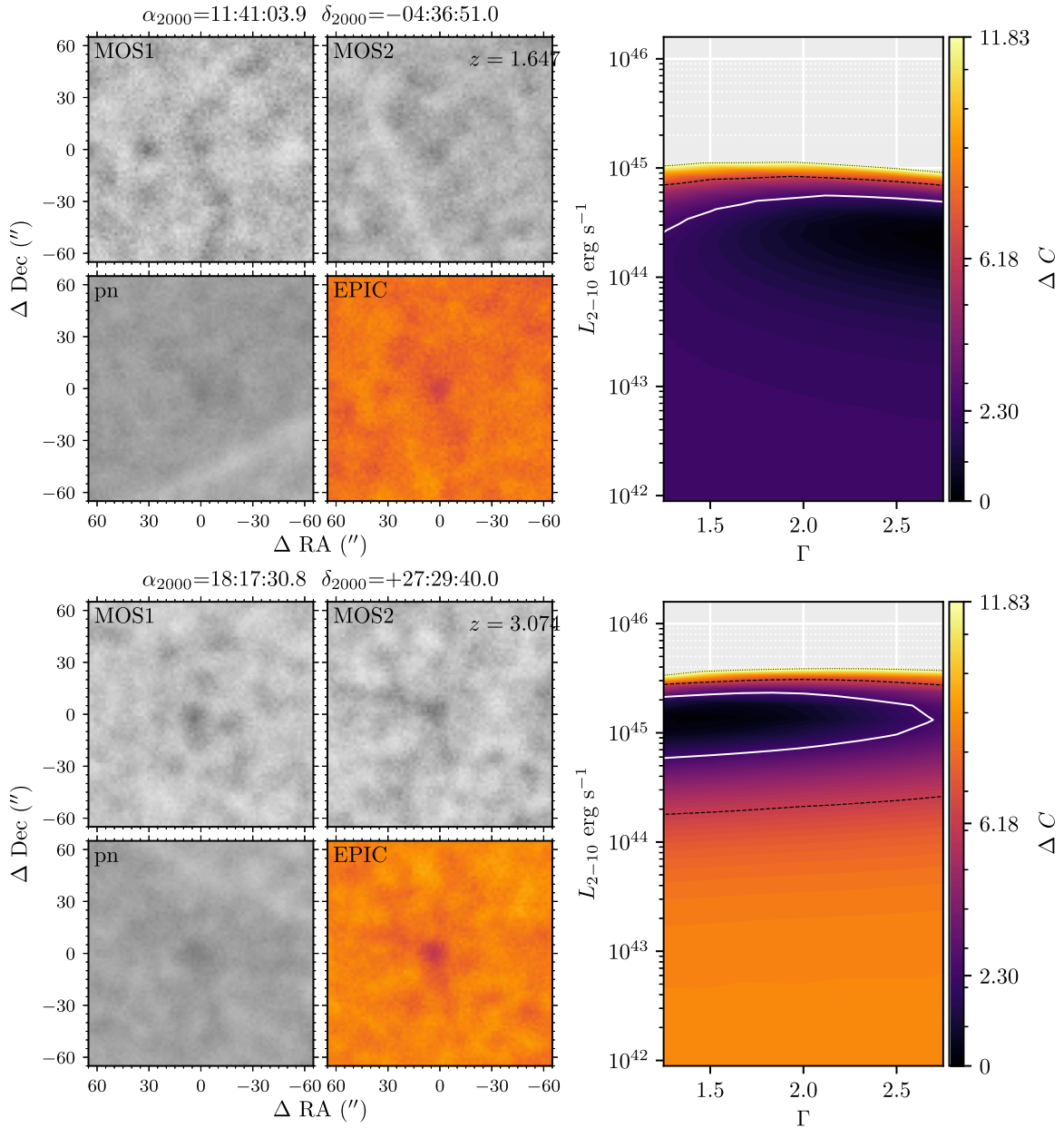


Figure 6. EPIC observations of SDSS J1141-0436 (top) and GraL J1817+2729 (bottom), in the same format as Figure 5. As these objects are not strongly detected, spectral fits are not shown—only the contours of upper limits on their X-ray luminosities.

ORCID iDs

Thomas Connor <https://orcid.org/0000-0002-7898-7664>
 Daniel Stern <https://orcid.org/0000-0003-2686-9241>
 Alberto Krone-Martins <https://orcid.org/0000-0002-2308-6623>
 S. G. Djorgovski <https://orcid.org/0000-0002-0603-3087>
 Matthew J. Graham <https://orcid.org/0000-0002-3168-0139>
 Dominic J. Walton <https://orcid.org/0000-0001-5819-3552>
 Ludovic Delchambre <https://orcid.org/0000-0003-2559-408X>
 Christine Ducourant <https://orcid.org/0000-0003-4843-8979>
 Ramachrisna Teixeira <https://orcid.org/0000-0002-6806-6626>
 Jakob Sebastian den Brok <https://orcid.org/0000-0002-8760-6157>
 Dougal Dobie <https://orcid.org/0000-0003-0699-7019>
 Laurent Galluccio <https://orcid.org/0000-0002-8541-0476>
 Priyanka Jalan <https://orcid.org/0000-0002-0524-5328>
 Sergei A. Klioner <https://orcid.org/0000-0003-4682-7831>
 Jonas Klüter <https://orcid.org/0000-0002-3469-5133>

Ashish A. Mahabal <https://orcid.org/0000-0003-2242-0244>
 Vibhore Negi <https://orcid.org/0000-0001-5824-1040>
 Anna Nierenberg <https://orcid.org/0000-0001-6809-2536>
 Sergio Scarano Jr <https://orcid.org/0000-0003-3739-4288>
 Dominique Sluse <https://orcid.org/0000-0001-6116-2095>
 Carolina Spíndola-Duarte <https://orcid.org/0000-0002-8052-7763>
 Jean Surdej <https://orcid.org/0000-0002-7005-1976>
 Joachim Wambsgans <https://orcid.org/0000-0002-8365-7619>

References

Agnello, A., Lin, H., Kuropatkin, N., et al. 2018, *MNRAS*, 479, 4345
 Arnaud, K. A. 1996, in ASP Conf. Ser. 101, *Astronomical Data Analysis Software and Systems V*, ed. G. H. Jacoby & J. Barnes (San Francisco, CA: ASP), 17
 Bañados, E., Mazzucchelli, C., Momjian, E., et al. 2021, *ApJ*, 909, 80
 Barret, D., Lam Trong, T., den Herder, J.-W., et al. 2018, *Proc. SPIE*, 10699, 106991G

- Barrett, P. E., & Bridgman, W. T. 1999, in ASP Conf. Ser. 172, *Astronomical Data Analysis Software and Systems VIII*, ed. D. M. Mehringer, R. L. Plante, & D. A. Roberts (San Francisco, CA: ASP), 483
- Bate, N. F., Floyd, D. J. E., Webster, R. L., & Wytthe, J. S. B. 2011, *ApJ*, 731, 71
- Bellm, E. C., Kulkarni, S. R., Graham, M. J., et al. 2019, *PASP*, 131, 018002
- Boese, F. G. 2000, *A&AS*, 141, 507
- Boller, T., Freyberg, M. J., Trümper, J., et al. 2016, *A&A*, 588, A103
- Brightman, M., Silverman, J. D., Mainieri, V., et al. 2013, *MNRAS*, 433, 2485
- Cash, W. 1979, *ApJ*, 228, 939
- Chartas, G., Cappi, M., Hamann, F., et al. 2016, *ApJ*, 824, 53
- Chen, B., Dai, X., Kochanek, C. S., et al. 2012, *ApJ*, 755, 24
- Chen, G. C. F., Chan, J. H. H., Bonvin, V., et al. 2018, *MNRAS*, 481, 1115
- Collett, T. E., Oldham, L. J., Smith, R. J., et al. 2018, *Sci*, 360, 1342
- Connor, T., Bañados, E., Stern, D., et al. 2019, *ApJ*, 887, 171
- Connor, T., Bañados, E., Mazzucchelli, C., et al. 2020, *ApJ*, 900, 189
- Connor, T., Bañados, E., Stern, D., et al. 2021, *ApJ*, 911, 120
- Courbin, F., Bonvin, V., Buckley-Geer, E., et al. 2018, *A&A*, 609, A71
- Dai, X., Kochanek, C. S., Chartas, G., et al. 2010, *ApJ*, 709, 278
- Delchambre, L., Krone-Martins, A., Wertz, O., et al. 2019, *A&A*, 622, A165
- Diego, J. M. 2019, *A&A*, 625, A84
- Dogrueel, M. B., Dai, X., Guerras, E., Cornachione, M., & Morgan, C. W. 2020, *ApJ*, 894, 153
- Ducourant, C., Wertz, O., Krone-Martins, A., et al. 2018, *A&A*, 618, A56
- Evans, P. A., Page, K. L., Osborne, J. P., et al. 2020, *ApJS*, 247, 54
- Fedorova, E. V., Zhdanov, V. I., Vignali, C., & Palumbo, G. G. C. 2008, *A&A*, 490, 989
- Fian, C., Mediavilla, E., Jiménez-Vicente, J., Muñoz, J. A., & Hansmeier, A. 2018, *ApJ*, 869, 132
- Fruscione, A., McDowell, J. C., Allen, G. E., et al. 2006, *Proc. SPIE*, 6270, 62701V
- Gabriel, C., Denby, M., Fyfe, D. J., et al. 2004, in ASP Conf. Proc. 314, *Astronomical Data Analysis Software and Systems XIII* (San Francisco, CA: ASP), 759
- Gaia Collaboration, Prusti, T., de Bruijne, J. H. J., et al. 2016, *A&A*, 595, A1
- Gaia Collaboration, Brown, A. G. A., Vallenari, A., et al. 2018, *A&A*, 616, A1
- Gandhi, P., Horst, H., Smette, A., et al. 2009, *A&A*, 502, 457
- Gehrels, N. 1986, *ApJ*, 303, 336
- Gibson, R. R., Jiang, L., Brandt, W. N., et al. 2009, *ApJ*, 692, 758
- Gilman, D., Du, X., Benson, A., et al. 2020, *MNRAS*, 492, L12
- Gordon, Y. A., Boyce, M. M., O'Dea, C. P., et al. 2020, *RNAAS*, 4, 175
- Guerras, E., Dai, X., Steele, S., et al. 2017, *ApJ*, 836, 206
- HI4PI Collaboration, Ben Bekhti, N., Flöer, L., et al. 2016, *A&A*, 594, A116
- Horst, H., Gandhi, P., Smette, A., & Duschl, W. J. 2008, *A&A*, 479, 389
- Jansen, F., Lumb, D., Altieri, B., et al. 2001, *A&A*, 365, L1
- Just, D. W., Brandt, W. N., Shemmer, O., et al. 2007, *ApJ*, 665, 1004
- Kellermann, K. I., Sramek, R., Schmidt, M., Shaffer, D. B., & Green, R. 1989, *AJ*, 98, 1195
- Kelly, P. L., Diego, J. M., Rodney, S., et al. 2018, *NatAs*, 2, 334
- Khorunzhev, G. A., Meshcheryakov, A. V., Medvedev, P. S., et al. 2021, *AsL*, 47, 123
- Khrantsov, V., Sergeyev, A., Spiniello, C., et al. 2019, *A&A*, 632, A56
- Kochanek, C. S., & Dalal, N. 2004, *ApJ*, 610, 69
- Kochanek, C. S., Falco, E. E., Impey, C. D., et al. 2000, *ApJ*, 535, 692
- Krone-Martins, A., Delchambre, L., Wertz, O., et al. 2018, *A&A*, 616, L11
- Krone-Martins, A., Graham, M. J., Stern, D., et al. 2019, arXiv:1912.08977
- Lamer, G., Schwobe, A., Wisotzki, L., & Christensen, L. 2006, *A&A*, 454, 493
- Lampton, M., Margon, B., & Bowyer, S. 1976, *ApJ*, 208, 177
- Lemon, C., Auger, M. W., McMahon, R., et al. 2020, *MNRAS*, 494, 3491
- Lemon, C. A., Auger, M. W., & McMahon, R. G. 2019, *MNRAS*, 483, 4242
- Lemon, C. A., Auger, M. W., McMahon, R. G., & Ostrovski, F. 2018, *MNRAS*, 479, 5060
- Li, J.-T., Decourchelle, A., Miceli, M., Vink, J., & Bocchino, F. 2015, *MNRAS*, 453, 3953
- Li, R., Napolitano, N. R., Tortora, C., et al. 2020, *ApJ*, 899, 30
- Luo, B., Brandt, W. N., Alexander, D. M., et al. 2014, *ApJ*, 794, 70
- Mereminskiy, I., Medvedev, P., Lutovinov, A., et al. 2020, *ATel*, 14206, 1
- Morgan, C. W., Kochanek, C. S., Dai, X., Morgan, N. D., & Falco, E. E. 2008, *ApJ*, 689, 755
- Mosquera, A. M., & Kochanek, C. S. 2011, *ApJ*, 738, 96
- Mosquera, A. M., Kochanek, C. S., Chen, B., et al. 2013, *ApJ*, 769, 53
- Nierenberg, A. M., Gilman, D., Treu, T., et al. 2020, *MNRAS*, 492, 5314
- Oguri, M., Rusu, C. E., & Falco, E. E. 2014, *MNRAS*, 439, 2494
- Ostrovski, F., McMahon, R. G., Connolly, A. J., et al. 2017, *MNRAS*, 465, 4325
- Ostrovski, F., Lemon, C. A., Auger, M. W., et al. 2018, *MNRAS*, 473, L116
- Paolillo, M., Schreier, E. J., Giacconi, R., Koekemoer, A. M., & Grogin, N. A. 2004, *ApJ*, 611, 93
- Paterno-Mahler, R., Sharon, K., Coe, D., et al. 2018, *ApJ*, 863, 154
- Pooley, D., Blackburne, J. A., Rappaport, S., & Schechter, P. L. 2007, *ApJ*, 661, 19
- Pooley, D., Rappaport, S., Blackburne, J. A., Schechter, P. L., & Wambsganss, J. 2012, *ApJ*, 744, 111
- Predehl, P., Andritschke, R., Arefiev, V., et al. 2021, *A&A*, 647, A1
- Read, A. M., Guainazzi, M., & Sembay, S. 2014, *A&A*, 564, A75
- Reis, R. C., Reynolds, M. T., Miller, J. M., & Walton, D. J. 2014, *Natur*, 507, 207
- Reynolds, M. T., Walton, D. J., Miller, J. M., & Reis, R. C. 2014, *ApJL*, 792, L19
- Ricci, C., Kara, E., Loewenstein, M., et al. 2020, *ApJL*, 898, L1
- Rodney, S. A., Balestra, I., Bradac, M., et al. 2018, *NatAs*, 2, 324
- Rusu, C. E., & Lemon, C. A. 2018, *RNAAS*, 2, 187
- Rusu, C. E., Oguri, M., Minowa, Y., et al. 2016, *MNRAS*, 458, 2
- Sartori, L. F., Schawinski, K., Trakhtenbrot, B., et al. 2018, *MNRAS*, 476, L34
- Schwobe, A., Semena, A., Maitra, C., et al. 2020, *ATel*, 14219, 1
- Stern, D. 2015, *ApJ*, 807, 129
- Stern, D., & Walton, D. J. 2020, *ApJL*, 895, L38
- Stern, D., Djorgovski, S. G., Krone-Martins, A., et al. 2021, *ApJ*, 921, 42
- Strüder, L., Briel, U., Dennerl, K., et al. 2001, *A&A*, 365, L18
- Sunyaev, R., Arefiev, V., Babyshkin, V., et al. 2021, *A&A*, 656, A132
- Suyu, S. H., Bonvin, V., Courbin, F., et al. 2017, *MNRAS*, 468, 2590
- Tomozeiu, M., Mohammed, I., Rabold, M., Saha, P., & Wambsganss, J. 2018, *MNRAS*, 475, 1925
- Treu, T. 2010, *ARA&A*, 48, 87
- Treu, T., Agnello, A., Baumer, M. A., et al. 2018, *MNRAS*, 481, 1041
- Turner, M. J. L., Abbey, A., Arnaud, M., et al. 2001, *A&A*, 365, L27
- Vega-Ferrero, J., Diego, J. M., Miranda, V., & Bernstein, G. M. 2018, *ApJL*, 853, L31
- Vegetti, S., Lagattuta, D. J., McKean, J. P., et al. 2012, *Natur*, 481, 341
- Vito, F., Brandt, W. N., Luo, B., et al. 2018, *MNRAS*, 479, 5335
- Voges, W., Aschenbach, B., Boller, T., et al. 2000, *IAUC*, 7432, 3
- Wachter, K., Leach, R., & Kellogg, E. 1979, *ApJ*, 230, 274
- Walsh, D., Carswell, R. F., & Weymann, R. J. 1979, *Natur*, 279, 381
- Walton, D. J., Reynolds, M. T., Miller, J. M., et al. 2015, *ApJ*, 805, 161
- Wayth, R. B., O'Dowd, M., & Webster, R. L. 2005, *MNRAS*, 359, 561
- Wertz, O., Stern, D., Krone-Martins, A., et al. 2019, *A&A*, 628, A17
- Wright, E. L., Eisenhardt, P. R. M., Mainzer, A. K., et al. 2010, *AJ*, 140, 1868